



# Optimization of current density of dye-sensitized solar cells by Cd substitution in the electron transport layer

M. I. Yasin<sup>1</sup> · Ghulam M. Mustafa<sup>2</sup> · M. I. Khan<sup>3</sup> · Badriah S. Almutairi<sup>4</sup> · Shamsa Kanwal<sup>3</sup> · A. Dahshan<sup>5</sup>

Received: 6 November 2023 / Revised: 25 March 2024 / Accepted: 20 April 2024  
© The Korean Ceramic Society 2024

## Abstract

This study addresses the growing need for energy worldwide and highlights the necessity of switching to sustainable options like dye-sensitized solar cells (DSSCs), which are well known for their affordability, ease of use, and competitive efficiency. Utilizing the sol-gel method, we synthesized diverse samples, including pristine TiO<sub>2</sub>, Cd-doped TiO<sub>2</sub>, and their heterostructures (TiO<sub>2</sub>@Cd-TiO<sub>2</sub>, Cd-TiO<sub>2</sub>@TiO<sub>2</sub>). A comprehensive evaluation encompassed structural, morphological, optical properties, and photovoltaic behavior through techniques like XRD, SEM, and UV-visible spectroscopy. Structural analysis highlighted the development of the anatase phase in all samples. The particles exhibited spherical grains, and heterostructures displayed dispersed particles with large sizes, enhancing electronic transport and dye absorption for efficient DSSCs. Cd-TiO<sub>2</sub>@TiO<sub>2</sub> exhibits the shortest bandgap (3.24 eV). Notably, Cd-TiO<sub>2</sub>@TiO<sub>2</sub> demonstrated favorable photovoltaic characteristics, including  $J_{sc}$  ( $8.65 \pm 0.2$  mA  $\text{cm}^{-2}$ ),  $V_{oc}$  ( $0.78 \pm 0.2$  V), FF ( $0.718 \pm 0.1$ ), and efficiency ( $4.848 \pm 0.5$ ). Electrochemical impedance spectroscopy (EIS) of TiO<sub>2</sub>@Cd-TiO<sub>2</sub> and Cd-TiO<sub>2</sub>@TiO<sub>2</sub> DSSCs unveiled distinct semicircles, indicating reduced charge transfer resistance and enhanced efficiency compared to TiO<sub>2</sub>-only DSSCs. This research contributes vital insights for advancing sustainable and efficient solar cell technologies.

**Keywords** Heterostructures · Anatase phase · Solar cell · Optical properties · Photovoltaic characteristics

## 1 Introduction

With the current rate of population increase, the global energy demand is projected to increase to 30 TW by the year 2050. High fossil fuel usage is causing serious environmental pollution and global warming, which triggered the scientific community to search for sustainable energy options [1]. Among the existing energy sources, which include tidal power, wind power, solar thermal power, and hydropower,

photovoltaic technology seems to be the most effective [2]. The solar cell, being a photovoltaic cell, is capable of converting sunlight directly into electrical energy [3]. However, the available materials for solar cell fabrications remained both a scientific opportunity and a challenge for researchers to have clean, inexpensive, and renewable energy [1]. The first commercially available solar cells were made of Pb and had a power conversion efficiency (PCE) of about 15–20% [4]. Though these compositions are highly stable, they are not exciting because of their carcinogenic nature. So there is an urgent need to substitute this Pb-based composition with some Pb-free compositions without compromising its stability and PCE. This aim opened a new debate among the scientific community to adopt new and novel strategies to synthesize next-generation solar cells. In the last decade, considerable work has been devoted to synthesizing the dye-sensitized solar cell (DSSC). The first dye-sensitized solar cell (DSSC) was reported by Grätzel and O'Regan, which received considerable interest from the researchers because of their high conversion efficiency up to ~10%, simplicity of manufacturing, and low cost of production [5]. The DSSC is a third-generation solar cell

✉ Badriah S. Almutairi  
bsalmutairi@pnu.edu.sa

<sup>1</sup> Acadiana Criminalistics Laboratory, New Iberia, LA, USA  
<sup>2</sup> Division of Science and Technology, Department of Physics, University of Education, Lahore 54770, Punjab, Pakistan  
<sup>3</sup> Department of Physics, University of Lahore, Lahore 53700, Pakistan  
<sup>4</sup> Department of Physics, College of Science, Princess Nourah bint Abdulrahman University, P.O. Box 84428, 11671 Riyadh, Saudi Arabia  
<sup>5</sup> Department of Physics, College of Science, King Khalid University, 61413 Abha, Saudi Arabia

with a production cost of roughly 1/3 to 1/5 times less than Si-based solar cells. The number of studies of metal complexes for photovoltaic applications has improved this efficiency. In DSSCs, the interaction of dye molecules with the porous thin film of a wide bandgap semiconductor plays a pivotal role in defining its efficiency. The material with sponge-like morphology and a larger surface area is an efficient choice for photoelectrodes. The efficiency of DSSC is fundamentally controlled by the transport capabilities of electrode materials and electron injection [6]. It has been reported that the number of electrons injected into wide-bandgap nanostructured semiconductors has a direct relationship with the overall conversion efficiency of DSSCs. So far, the small cells currently exhibit a record efficiency of around 11.1%, and large-scale experiments have made it clear how urgent the commercialization of DSSCs is. As a result, DSSCs are superior to Si-based solar cells in terms of (i) position of the dye's border molecular orbitals, i.e., HOMO and LUMO, (ii) Fermi level of scaffold material, and (iii) redox potential of electrolyte [7]. The dye molecule's HOMO and LUMO energy gaps should be small enough that photon absorption can easily excite electrons from the ground to an excited state. For uninterrupted electron flow from dye to  $\text{TiO}_2$  material, the LUMO of the dye molecule must lie below the conduction band of  $\text{TiO}_2$ . The electronic transfer from photoanode to counter electrode makes the working of the DSSC very interesting, as shown in Fig. 1.

The central part of the DSSCs is the mesoscopic semiconductor oxide sheet that is in contact with either an organic hole conductor or a redox electrolyte. The monolayer of dye sensitizer is affixed to the film of nanocrystalline material. When exposed to sunlight, the dye sensitizer absorbs a photon (light), and if the energy of the photon is sufficient to promote electrons of dye molecules from the HOMO to the LUMO level, it becomes photoexcited. The holes present in dye molecules at the interface and electrons in  $\text{TiO}_2$  set up the charge separation that is essential for DSSCs to work. The dye molecules adsorbed at the surface

provide electrons from the LUMO level of dye to the anatase phase of  $\text{TiO}_2$ , which has smaller energy levels than the excited state of dye molecules [9].

The rear contact of the working electrode becomes active when the charge collection takes place after the electrons have been transported via the porous  $\text{TiO}_2$  network. When these charged particles return to the counter electrode, the Pt coated on the FTO substrate in the form of  $\text{Pt}^{2+}$  captures these incoming electrons and reduces them to Pt. This Pt once again oxidizes by donating one electron to the iodine electrolyte, which is ready to perform the redox reaction and thus regenerate dye molecules [10]. The iodine molecule ( $\text{I}_2$ ) and iodide ion ( $\text{I}^-$ ), are typically united to form  $\text{I}_3^-$  in the electrolyte. Iodide ions ( $3\text{I}^-$ ) are formed during the process of accepting electrons from the counter electrode [11]. These ions are oxidized again by giving electrons to the dye, which yields triiodide ions. Finally, the liquid electrolyte will reduce the oxidized dye and thus complete the reaction. The voltage produced during this process is determined by the electrolyte's redox potential and the electron Fermi level of solids. In general, the device produces electric power from light without undergoing any long-term chemical changes [12].  $\text{MoO}_3$ ,  $\text{SnWO}_4$ ,  $\text{CuWO}_4$ ,  $\text{TiO}_2$ , and  $\text{V}_2\text{O}_5$  are the dye-sensitized nanocrystalline semiconductor photoanodes used in DSSCs. The stability of  $\text{TiO}_2$  in three different phases, anatase, rutile, and brookite, makes the  $\text{TiO}_2$ -based DSSCs the most astounding among all available options. The high chemical stability, high conduction band edge energy (3.2 eV), and low synthesis temperature make the anatase phase very attractive for the photoanode in DSSC. Rutile's conduction band edge energy, in contrast, is around 3 eV [13]. Due to the high packing density of rutile  $\text{TiO}_2$ , which prevents electron transmission, anatase-based DSSCs produce a 30% higher short circuit current than rutile-based DSSCs for the same film thickness [2].  $\text{TiO}_2$  is a good photoanode, although its efficiency is constrained by a high recombination rate. To lower the recombination rate and current density of  $\text{TiO}_2$ , doping has been one of the methods that has received the most attention.  $\text{TiO}_2$  has already been reported to be modified by dopants such as Cd, Ni, Cu, Zn, Co, Sn, W, Fe, and Au for specific and intended uses. To solve the problem of quick recombination and increase the current density of DSSCs, doping with Cd is suggested as the optimum crystal-modified element. Cadmium (Cd) is a suitable dopant for titanium dioxide ( $\text{TiO}_2$ ) owing to its specific properties and compatibility with the crystal lattice of  $\text{TiO}_2$ . A key factor in its suitability is the ionic radius of Cd, which, at 0.97 Å, is very similar to the ionic radius of titanium ( $\text{Ti}^{4+}$ ) ions in  $\text{TiO}_2$ . This similarity enables Cd to seamlessly substitute for Ti in the crystal lattice. The introduction of Cd into the  $\text{TiO}_2$  lattice creates new energy levels within the bandgap, leading to a modification of the material's electronic structure. This alteration plays a crucial

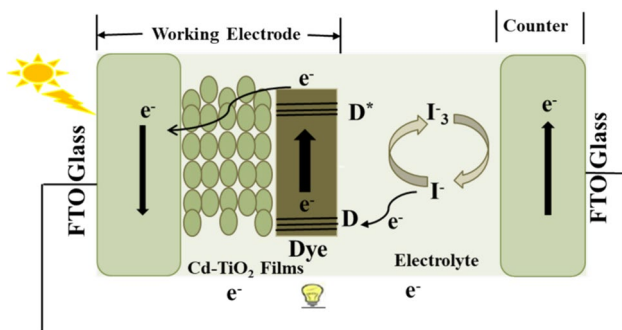


**Fig. 1** Schematic diagram of the working principle of DSSCs (adopted from [8])

role in diminishing the rate of electron–hole recombination, a significant factor in enhancing the efficiency of optoelectronic devices utilizing  $\text{TiO}_2$ , such as solar cells or photocatalysts. Furthermore, experimental findings validate that Cd doping in  $\text{TiO}_2$  markedly improves the absorption of visible light and facilitates a more efficient transfer of electrons across the interface. The notable enhancement in solar cell performance observed with Cd doping is predominantly ascribed to the increased short-circuit current density ( $J_{sc}$ ). The augmented  $J_{sc}$  signifies that more electrons are effectively generated, contributing to an enhanced photocurrent and ultimately resulting in higher overall efficiency in solar energy conversion. The heterostructure also suppresses the rate of recombination through doping. The lattice mismatching is crucial when creating heterostructures because most of the time heterostructure formulism makes the structure unstable [8]. To overcome this challenge, we created a heterostructure comprising pure and doped material using a straightforward procedure. The material in this kind of heterostructure is highly crystalline and stable. Additionally, since the electrolyte is exposed to two layers, corrosion will be minimal. The other layer will continue to connect the cell if one layer is damaged by the electrolyte. Meanwhile, the heterostructure prevents the electrolyte from contacting the FTO and creating a short circuit. To lower the recombination rate and increase the current density, Cd– $\text{TiO}_2$ @ $\text{TiO}_2$  heterostructures have been fabricated, which pave the path to stable heterostructure design for additional electrochemical and optoelectronic devices and open a new debate for the research community. The broad research scope that this study presents creates opportunities for the developed technologies to be applied in a variety of optoelectronic devices. Apart from the direct focus on dye-sensitized solar cells (DSSCs), various optoelectronic applications may benefit from the knowledge gathered from the study of Cd-doped  $\text{TiO}_2$  and Cd– $\text{TiO}_2$ @ $\text{TiO}_2$  heterostructures. These could be sensors, light-emitting diodes (LEDs), photodetectors, and photocatalysts, among others. The distinct characteristics and improved performance noted in the context of solar cells imply that these materials and heterostructures may find flexible applications in a variety of devices, thereby advancing a range of optoelectronic technologies. The results of this study pave the way for additional investigation and debate among scientists, fostering cooperative endeavors to fully use these materials' potential in tackling complex problems and strengthening the discipline of optoelectronics. The heterostructure also suppresses the rate of recombination through doping. The lattice mismatching is crucial when creating heterostructures because most of the time heterostructure formulism makes the structure unstable. To overcome this challenge, we created a heterostructure comprising pure and doped material using a straightforward

procedure. The material in this kind of heterostructure is highly crystalline and stable. Additionally, since the electrolyte is exposed to two layers, corrosion will be minimal. The other layer will continue to connect the cell if one layer is damaged by the electrolyte. Meanwhile, the heterostructure prevents the electrolyte from contacting the FTO and creating a short circuit. To lower the recombination rate and increase the current density, Cd– $\text{TiO}_2$ @ $\text{TiO}_2$  heterostructures have been fabricated, which pave the path to stable heterostructure design for additional electrochemical and optoelectronic devices and open a new debate for the research community.

## 2 Experimental setup

### 2.1 Material synthesis

#### 2.1.1 Synthesis of titanium dioxide ( $\text{TiO}_2$ )

The sol–gel method was employed for the synthesis of  $\text{TiO}_2$ . In this process, 20 ml of titanium tetraisopropoxide was combined with 20 ml of ethanol through continuous stirring for 7–10 min. Simultaneously, a second solution was prepared by mixing 24 ml of nitric acid ( $\text{HNO}_3$ ) with 8 ml of distilled water. This second solution was then added to the homogeneous titanium-containing mixture. The entire combination formed a gel as a result of continuous stirring. To complete the drying process, the gel was placed in an oven set at 80 °C for 3 h. After the drying process, a white precipitate was produced, which was then finely turned into a powder. This white-colored fine powder was then placed into a muffle furnace and annealed at 450 °C for 2 h. The material was removed from the furnace and processed again until fine nanoparticles were obtained.

#### 2.1.2 Synthesis of cadmium-doped titanium dioxide (Cd– $\text{TiO}_2$ )

For Cd doping, the sol–gel method was employed. 20 ml of titanium tetraisopropoxide (TTIP) and 20 ml of ethanol were stirred for 10 min. Subsequently, 3% of 0.1 M  $\text{CdCl}_2$  was introduced into this solution through continuous stirring. A mixture of 24 ml of nitric acid ( $\text{HNO}_3$ ) and 8 ml of deionized water (D.I. water) was added to the solution, and continuous stirring for 30 min resulted in the formation of a gel. The gel was then dried in an oven at 80 °C for 3 days. After drying, the powder was annealed at 450 °C for 2 h in a muffle furnace. Following the annealing process, the doped material was crushed to produce fine nanoparticles of Cd– $\text{TiO}_2$ .

### 2.1.3 Synthesis of heterostructures (TiO<sub>2</sub>@Cd-TiO<sub>2</sub> and Cd-TiO<sub>2</sub>@TiO<sub>2</sub>)

Heterostructures were synthesized using cadmium-doped titanium dioxide (Cd-TiO<sub>2</sub>), titanium dioxide (TiO<sub>2</sub>), and distilled water. For the fabrication of TiO<sub>2</sub>@Cd-TiO<sub>2</sub>, a solution of 0.1 mol of TiO<sub>2</sub> was initially prepared, and then nanoparticles of Cd-TiO<sub>2</sub> (0.1 mol) were added. The process was repeated, followed by drying to obtain a fine powder. Similarly, for the fabrication of Cd-TiO<sub>2</sub>@TiO<sub>2</sub>, a solution of 0.1 mol of Cd-TiO<sub>2</sub> was first prepared, and nanoparticles of TiO<sub>2</sub> (0.1 mol) were added. The same drying process was repeated to obtain a fine powder.

### 2.1.4 Characterizations

Using a  $CuK_{\alpha}$  source with a 1.5406 Å wavelength, the Bruker D8 X-ray diffractometer was used to determine the crystal structure. The operating voltage and current used for this characterization were 40 kV and 100 mA, respectively. Field emission scanning electron microscopy was used to analyze the materials' surface morphology (FE-SEM, Nova-450). The optical properties of the materials were assessed using the spectrophotometer Agilent 8453.

## 2.2 Cell fabrication and photovoltaic measurements

For photovoltaic measurement, the cell assembly is designed by pasting the pristine and Cd-doped TiO<sub>2</sub>, TiO<sub>2</sub>@Cd-TiO<sub>2</sub>, and Cd-TiO<sub>2</sub>@TiO<sub>2</sub> nanostructures on FTO glass substrates using a doctor blade. The electrodes were sintered for 120 min at 450 °C, and these sintered samples were soaked in a Ru dye and ethanol solution for 24 h. The platinum paste was used to make the collector electrodes. To facilitate the redox process, a mixture of 0.5 M LiI, 0.05 M I<sub>2</sub>, 0.6 M TBP, and 0.6 M HMII in MPN were employed. To perform solar cell testing, a Keithley 2611 source meter (Keithley Instruments, Inc.) was used, and a solar simulator AM 1.5 was used for incident light with an intensity of 100 mW cm<sup>-2</sup>, and the working area for all these measurements was limited to 0.2 cm<sup>2</sup>.

## 3 Results and discussion

### 3.1 X-ray diffraction analysis

Figure 2 displays the XRD peaks of the synthesized samples in the 20–70°, 2θ range. These XRD patterns were indexed, and the Miller indices corresponding to these diffraction peaks are mentioned on top. These Miller indices were (101), (004), (200), (211), and (213) corresponding to the

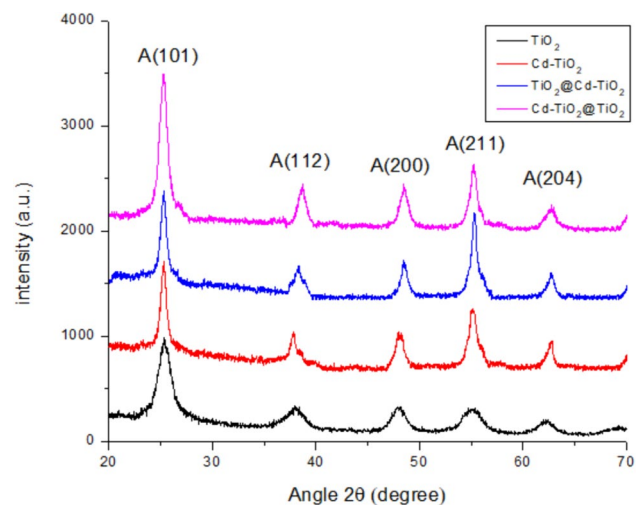


**Fig. 2** X-ray diffraction analysis patterns of TiO<sub>2</sub>, Cd-TiO<sub>2</sub>, TiO<sub>2</sub>@Cd-TiO<sub>2</sub> and Cd-TiO<sub>2</sub>@TiO<sub>2</sub>

X-ray diffraction peaks that appeared at 25.33, 37.95, 48.02, 55.17, and 62.33 2θ values. It has been observed that these peaks were well matched with the PDF card # 21-1272 and confirmed the formation of the anatase phase of TiO<sub>2</sub>. In Cd-TiO<sub>2</sub> samples, the same Miller indices were observed while the peaks were little shifted toward the smaller angle, and the intensity of the peak increased. No other peaks related to Cd-Ti, CdO, etc. were seen, which is an undeniable evidence that Cd was doped into TiO<sub>2</sub> without bringing any structural distortion. No other peak can be seen in the Cd-TiO<sub>2</sub> graph, which is an undeniable evidence that Cd was doped into TiO<sub>2</sub> without bringing any structural distortion. The stability of the anatase phase persists even in the formation of heterostructures, as can be witnessed from the XRD patterns of TiO<sub>2</sub>@Cd-TiO<sub>2</sub> and Cd-TiO<sub>2</sub>@TiO<sub>2</sub>. This high-intensity peak is observed by the sample of Cd-TiO<sub>2</sub>@TiO<sub>2</sub>, which showed high intensity.

According to published reports, a high dopant concentration may result in the accumulation of dopants and can give rise to some new phases [14]. It is important to note that even with heterostructure semiconductor materials, no rutile peak was seen. The emerging peaks in all four materials maintain the same planes with Miller indices of (101), (004), (200), (211), and (213), which are identical to those of pristine TiO<sub>2</sub>. However, with doping, the peaks grow more pronounced and narrower, and particularly the heterostructure materials show increased tilting toward lower angles. This is the first success of this work to grow the pristine TiO<sub>2</sub>, Cd-TiO<sub>2</sub>, TiO<sub>2</sub>@Cd-TiO<sub>2</sub>, and Cd-TiO<sub>2</sub>@TiO<sub>2</sub> heterostructures, and these heterostructures have great potential for DSSC applications [15].

Crystallite size is one of the key structural parameters that determines the extent of crystal growth and is usually

calculated using Scherrer's formula:  $D = 0.9\lambda/\beta\cos\theta$ , where  $\theta$ ,  $\beta$ , and  $\lambda$  are diffraction angle, full width at half maxima, and wavelength of incident X-rays. In addition, the value 0.9 is the shape factor. Since the value of crystallite size is directly linked to the peak's shape, a larger peak corresponds to a larger crystallite size. It has been noticed that Cd doping made the peak thinner, which reflects the growth of crystallite size. Similarly, in the formation of heterostructures, the peaks became sharper, which proved that the heterostructure formation approach is a suitable option to get a larger crystallite size. The same type of attempt is made in the literature by choosing different dopants such as Zn, Sn, and Cr and observing smaller crystallite sizes [16]. A larger crystallite size facilitates electronic transportation by minimizing the charge trap at the grain boundaries and thus improving the device's efficiency. In addition, this increase in grain size will decrease the charge trapping sites noticeably and yield a better current density [17]. It has been proposed that the material with a larger crystallite size is preferable for DSSC applications, and there might have been some favorable conditions for the production of larger particle sizes in the absence of any other TiO<sub>2</sub> phases [18].

X-ray diffraction is a powerful technique that can be used to calculate the  $d$ -spacing of any crystalline material. The  $d$ -spacing for pristine TiO<sub>2</sub> was noticed at 3.50 Å which slightly increased to 3.51 Å for Cd–TiO<sub>2</sub>. This slight increase in  $d$ -spacing has been attributed to the incorporation of Cd at the interstitial sites [19]. For both heterostructures: TiO<sub>2</sub>@Cd–TiO<sub>2</sub> and Cd–TiO<sub>2</sub>@TiO<sub>2</sub> the  $d$ -spacing is further increased and noted as 3.52 Å. Identical  $d$ -spacing value for heterostructures indicates that these formalisms grow in a quite similar fashion and that new materials with comparable structures have formed. In addition, this increase in  $d$ -spacing is also consistent with a slight shifting of peaks in X-ray diffraction patterns [20].

Table 1 summarizes the calculated values of lattice parameters, and interestingly, it has been observed that the unit cell of pure TiO<sub>2</sub> expanded a little when it accommodated Cd. This increase in lattice parameters is associated with the larger ionic radii of Cd<sup>2+</sup> as compared with Ti<sup>4+</sup>. It is intriguing that the parameter  $a$  is compressed

when heterostructures are formulated, whereas the parameter  $c$  is noticeably extended. A novel environment for charge transport is provided by these modified parameters in addition to the production of new materials. Modified lattice parameters considerably reduce the rate of charge recombination [21, 22].

### 3.2 Scanning electron microscopy analysis

Figure 3 displays the SEM images of TiO<sub>2</sub>, Cd–TiO<sub>2</sub>, TiO<sub>2</sub>@Cd–TiO<sub>2</sub>, and Cd–TiO<sub>2</sub>@TiO<sub>2</sub> samples captured at 100,000× magnification which uncovered the minor details of the surface of the sample and provided better estimation regarding the particles size, particle's distribution, surface roughness, and texture. For the parent composition, that is, the pristine TiO<sub>2</sub> exhibited well-shaped spherical grains with sharp and distinct boundaries. These particles are well connected, leaving behind little pores. The particle size was estimated using the Java-based software ImageJ, and the average particle size was found to be 53 nm, as shown in Fig. 3a. When a small amount of Cd is doped, it increases the surface energy and facilitates particle agglomeration, which is evident from Fig. 3b. However, using the heterostructure formalism, we obtained particle dispersion in densely stacked layers, which provides a better opportunity for electronic transportation, as shown in Fig. 3c and d. This unpolished surface is more absorbent for dye and, therefore, thought to be better suited for effective DSSCs [23].

### 3.3 UV–Vis analysis

The absorbance capabilities of the four semiconductor materials, TiO<sub>2</sub>, Cd–TiO<sub>2</sub>, TiO<sub>2</sub>@Cd–TiO<sub>2</sub>, and Cd–TiO<sub>2</sub>@TiO<sub>2</sub>, were evaluated by recording their absorption spectra using a UV–visible spectroscope. Any semiconductor material used to fabricate the photoanode for the DSSC is supposed to be a good absorber [24]. The absorption spectrum for heterostructures is shown in Fig. 4a. The absorbance spectra revealed that Cd doping increased the absorption of pure TiO<sub>2</sub>, which is attributed to the localized electron exchange activity [25]. However, the conduction barrier of TiO<sub>2</sub> is controlled by the 3d electrons. In the case of heterostructure formation, TiO<sub>2</sub>@Cd–TiO<sub>2</sub> and Cd–TiO<sub>2</sub>@TiO<sub>2</sub>, the effect of absorbance favorability becomes more pronounced. Increased absorbance below the UV region is significantly influenced by the absence of the rutile phase [26]. The change in absorbance is primarily attributed to heterostructures' increased grain size and lattice parameters [27]. Upon observing the morphology of Cd–TiO<sub>2</sub>@TiO<sub>2</sub> (Fig. 3c), it is evident that its surface is remarkably smooth in comparison to the others. Additionally, both SEM and XRD analyses indicate a larger grain size for this film. The quantum confinement effect comes into play, where a higher

**Table 1** Lattice parameters of pristine TiO<sub>2</sub>, Cd–TiO<sub>2</sub>, TiO<sub>2</sub>@Cd–TiO<sub>2</sub> and Cd–TiO<sub>2</sub>@TiO<sub>2</sub> nanostructures

Photoanode	Lattice parameters	
	$a = b$ (Å)	$c$ (Å)
TiO <sub>2</sub>	3.78	7.07
Cd–TiO <sub>2</sub>	3.80	7.2
TiO <sub>2</sub> @Cd–TiO <sub>2</sub>	3.76	10
Cd–TiO <sub>2</sub> @TiO <sub>2</sub>	3.76	10

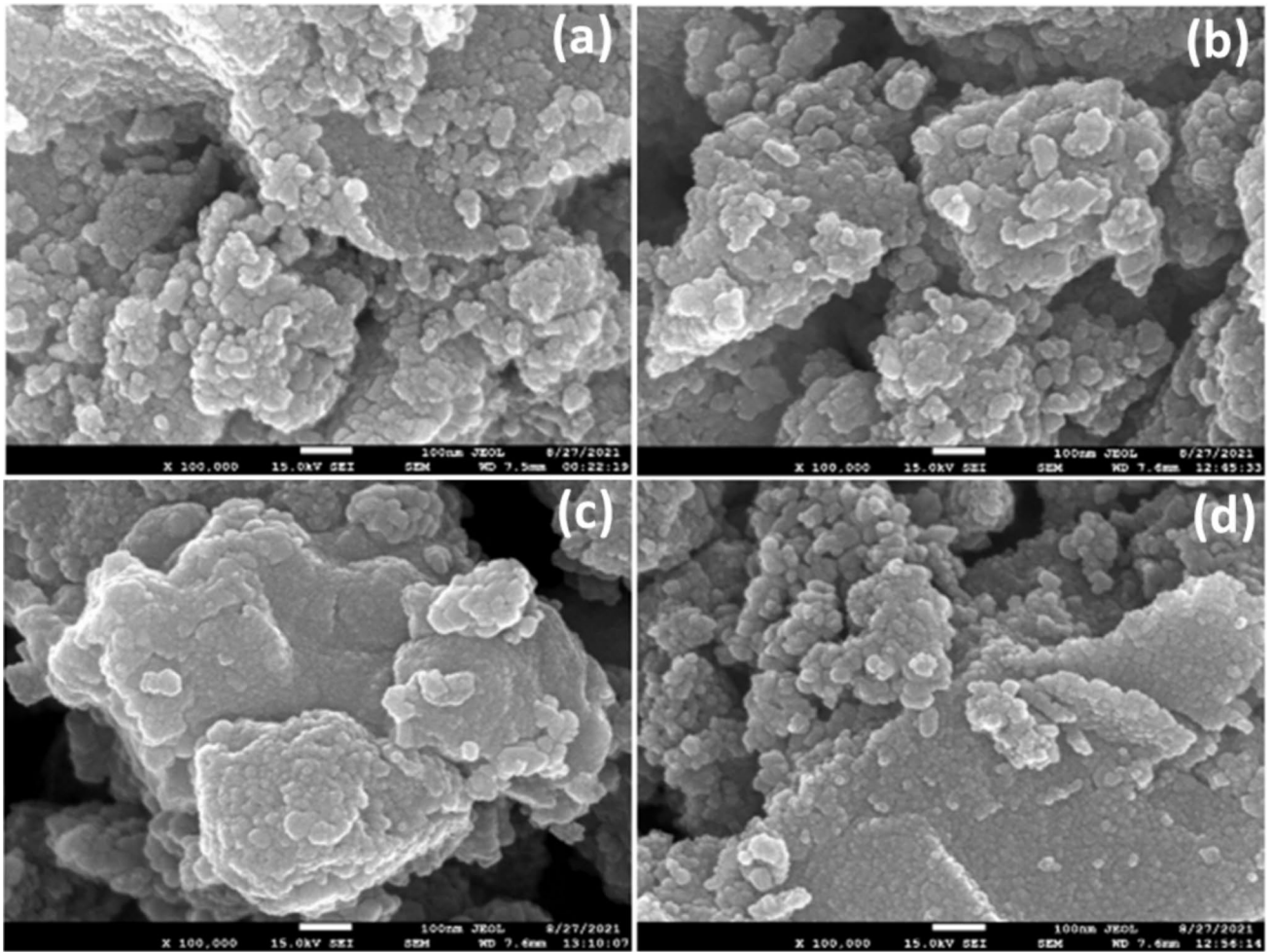


Fig. 3 SEM images of  $\text{TiO}_2$ ,  $\text{Cd-TiO}_2$ ,  $\text{TiO}_2@Cd-TiO_2$  and  $\text{Cd-TiO}_2@TiO_2$  films

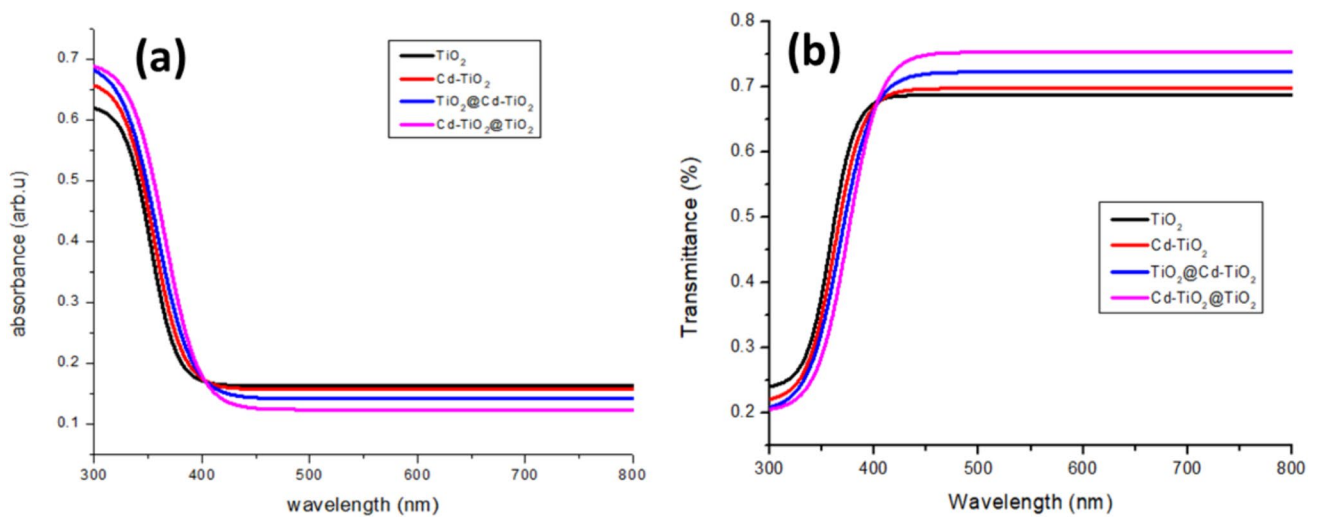


Fig. 4 Absorbance and transmission spectra of  $\text{TiO}_2$ ,  $\text{Cd-TiO}_2$ ,  $\text{TiO}_2@Cd-TiO_2$  and  $\text{Cd-TiO}_2@TiO_2$  heterostructures

grain size leads to a smaller bandgap energy and a shift in the absorbance peak towards longer wavelengths. Therefore, the absorbance of the Cd–TiO<sub>2</sub>@TiO<sub>2</sub> sample is high. The best properties for absorbance in heterostructures are shown by Cd–TiO<sub>2</sub>@TiO<sub>2</sub>.

The transmission capability of each semiconductor was evaluated, and the results are shown in Fig. 4b. For photoanode materials, high transmittance in the visible portion of the spectrum is a highly desirable property [28]. Figure 4b depicts a visible region with a relatively high transmittance. Comparatively speaking, the heterostructures revealed better transmission in the visible range of the electromagnetic spectrum, and the highest value of transmission is recorded for Cd–TiO<sub>2</sub>@TiO<sub>2</sub>, which makes this composition adequate for DSSC applications. The high transmission reflects the ability of semiconductors to generate charges for the functioning of DSSCs [29].

### 3.4 Dielectric constant

The real ( $\epsilon_r$ ) and imaginary ( $\epsilon_i$ ) parts of the dielectric constant for all the samples are presented in Fig. 5.  $\epsilon_r$  is associated with the absorption of the material, and a material having a larger value of  $\epsilon_r$  is a good absorber. It is evident from Fig. 5a that all samples reveal good absorption in the UV region of the electromagnetism spectrum, which supports the finding of absorbance spectra. However, in the visible range, the value of  $\epsilon_r$  is small and reflects a small reflection in this region. The imaginary part of the dielectric constant determines the dispersion of light from the material. It is observed that the trend of  $\epsilon_i$  is somehow identical to that of  $\epsilon_r$ . It means pure and Cd-doped TiO<sub>2</sub> as well as heterostructure compositions show good absorption as well as good dispersion in the UV region of the spectrum.

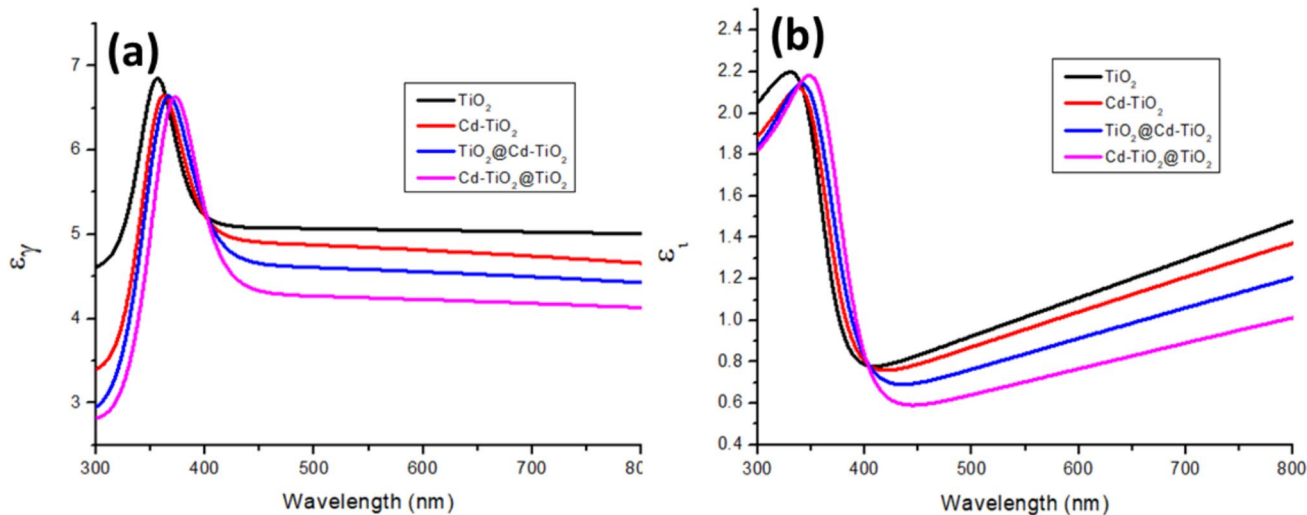


Fig. 5 Real and imaginary parts of dielectric constant for TiO<sub>2</sub>, Cd–TiO<sub>2</sub>, TiO<sub>2</sub>@Cd–TiO<sub>2</sub> and Cd TiO<sub>2</sub>@TiO<sub>2</sub> heterostructures

### 3.5 Refractive index

The refractive index is one of the key optical parameters that quantifies the response of a material to external light, and it depends upon the polarization of ions present inside them and the local electric field. The refractive index ( $n$ ) is linked with the reflection ( $R$ ) and extinction coefficient ( $k$ ) as:

$$n = \left( \frac{1+R}{1-R} \right) + \sqrt{\frac{4R}{(1-R)^2} - k^2}. \quad (1)$$

The value of  $n$  versus the wavelength of incident light is plotted in Fig. 6, which shows a peak value in the UV region and then becomes constant in the visible spectrum of light. According to Fig. 6, the refractive index of all

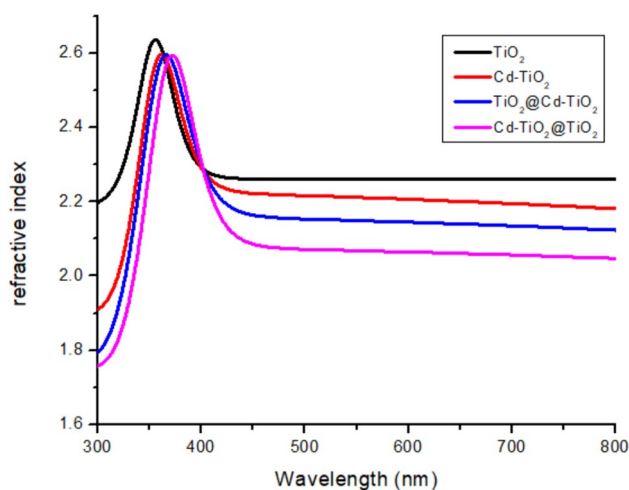


Fig. 6 Refractive index ( $n$ ) of TiO<sub>2</sub>, Cd–TiO<sub>2</sub>, TiO<sub>2</sub>@Cd–TiO<sub>2</sub>, and Cd–TiO<sub>2</sub>@TiO<sub>2</sub> films

materials increases with the increase in wavelength, reaches a maximum value, and then begins to fall. The lowest refractive index is shown by the semiconductor material Cd–TiO<sub>2</sub>@TiO<sub>2</sub>, while the highest refractive index is shown by pure TiO<sub>2</sub>. After reaching a particular maximum value, the value of  $n$  began to decrease. This decrease in the value of  $n$  is attributed to the decrease in surface optical dispersion and optical losses. These optical losses are caused by increased charge concentration and decreased surface roughness due to newly produced materials as a result of doping [30–32]. When compared to non-heterostructure materials, heterostructure materials such as TiO<sub>2</sub>@Cd–TiO<sub>2</sub> and Cd–TiO<sub>2</sub>@TiO<sub>2</sub> show reduced refractive responses.

### 3.6 Optical bandgap

The optical bandgap ( $E_g$ ) is the most important parameter, which plays a pivotal role in controlling the optical conductivity of the material. The analysis of the Tauc plot is an appropriate way to estimate the bandgap values, which are presented in Fig. 7. The value of  $E_g$  for TiO<sub>2</sub> was noticed as 3.43 eV, and when a nominal amount of Cd was incorporated, the value of  $E_g$  was slightly reduced to 3.32 eV. This reduction of bandgap value shows the ease of electronic transition from the valence to the conduction band that is attributed to the creation of new dopant levels in the bandgap by the inclusion of Cd doping [33]. In addition, the introduction of Cd into TiO<sub>2</sub> creates some electron capture and thus helps to suppress electron–hole recombination [34]. The bandgap value was further reduced for heterostructure formulism, and it was noticed as 3.28 eV, and 3.24 eV for TiO<sub>2</sub>@Cd–TiO<sub>2</sub>, and Cd–TiO<sub>2</sub>@TiO<sub>2</sub>, respectively.

Furthermore, the red shift in the absorption edges indicates that the bandgap of Cd–TiO<sub>2</sub>@TiO<sub>2</sub> is the smallest, while that of pure TiO<sub>2</sub> is the largest. When heterostructures

are produced, the bandgap is slightly reduced since the rutile phase is not present. The inherent properties, in conjunction with enhanced light sensitivity in the visible region, are made possible by the presence of a Cd dopant in Cd–TiO<sub>2</sub>@TiO<sub>2</sub>. The increased light scattering and absorption are made possible by the narrow bandgap [35].

### 3.7 Photovoltaic performance

Figure 8 shows the  $J$ – $V$  characteristics of various DSSCs nanostructures, and these graphs were used to calculate the key performance parameters like open circuit voltages ( $V_{oc}$ ), current density ( $J_{sc}$ ), and fill factor (FF) and the calculated values of all these factors are provided in Table 2. The calculation of  $J_{sc}$  involves the initial number of photogenerated carriers, the recombination rate of electron–hole pairs, and injection efficiency. The recombination rate depends on the number of injected electrons, redox species, and oxidized dye molecules. The open circuit voltage, fill factor, and efficiency are calculated as:

$$V_{oc} = |E_F - E_{redox}| \quad (2)$$

$$\eta = \frac{FF \times V_{oc} \times J_{sc}}{P_{in}}, \quad (3)$$

$$FF = \frac{I_{max} \times V_{max}}{J_{sc} \times V_{oc}}. \quad (4)$$

Here,  $E_F$  is the fermi level and  $E_{redox}$  depends upon the energy levels of electrolyte, i.e., ( $I^-/I_3^-$ ). In addition,  $P_{in}$ ,  $I_{max}$ , and  $V_{max}$  are input power, maximum current, and

**Fig. 7** Energy bandgap of TiO<sub>2</sub>, Cd–TiO<sub>2</sub>, TiO<sub>2</sub>@Cd–TiO<sub>2</sub> and Cd–TiO<sub>2</sub>@TiO<sub>2</sub> films

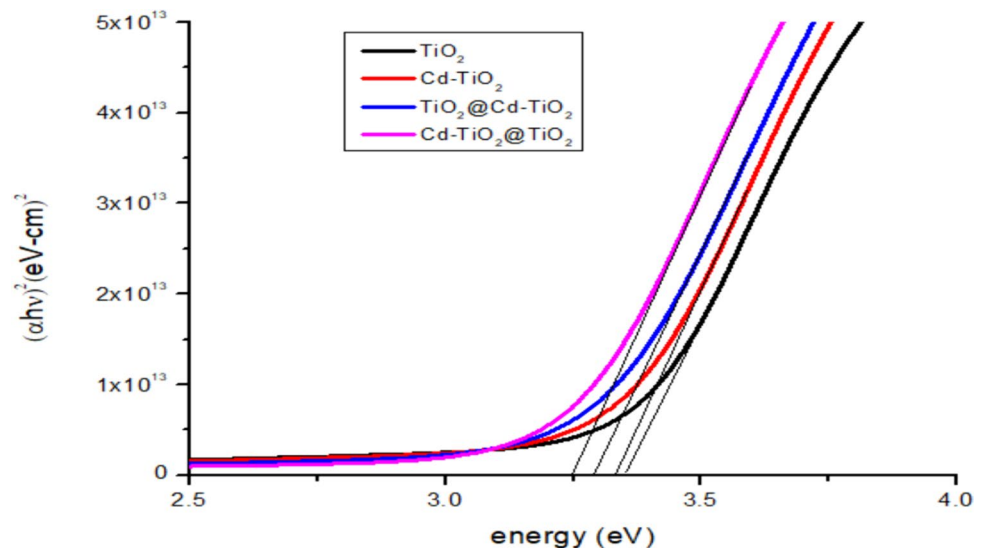




**Fig. 8**  $J$ - $V$  measurement of  $\text{TiO}_2$ ,  $\text{Cd-TiO}_2$ ,  $\text{TiO}_2@$   $\text{Cd-TiO}_2$  and  $\text{Cd-TiO}_2@$   $\text{TiO}_2$  photoanodes-based dye-sensitized solar cells

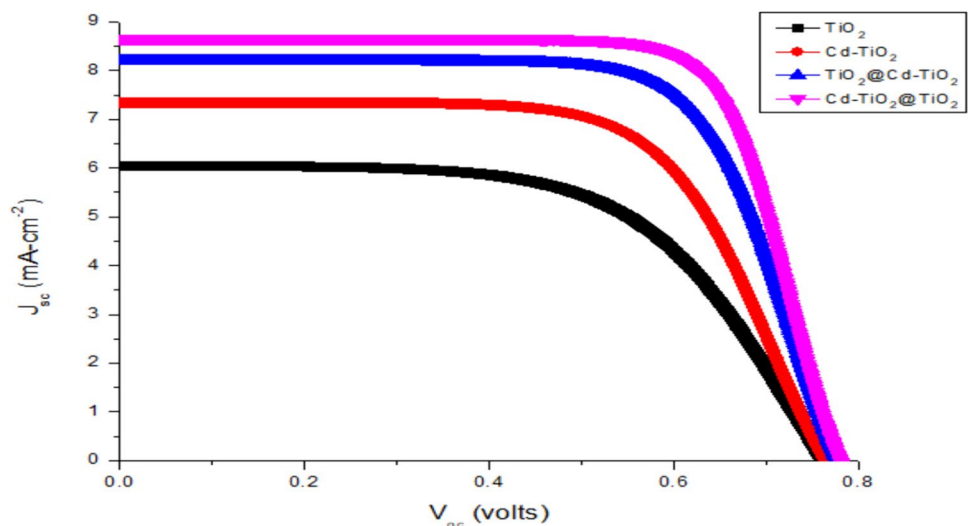


**Table 2** Parameters of different DSSCs

Samples	$J_{sc}$ ( $\text{mA cm}^{-2}$ )	$V_{oc}$ (V)	FF	$\eta\%$
$\text{TiO}_2$	$6.04 \pm 0.2$	$0.76 \pm 0.2$	$0.571 \pm 0.1$	$2.622 \pm 0.5$
$\text{Cd-TiO}_2$	$7.35 \pm 0.2$	$0.762 \pm 0.2$	$0.653 \pm 0.1$	$3.66 \pm 0.5$
$\text{TiO}_2@$ $\text{Cd-TiO}_2$	$8.19 \pm 0.2$	$0.777 \pm 0.2$	$0.713 \pm 0.1$	$4.543 \pm 0.5$
$\text{Cd-TiO}_2@$ $\text{TiO}_2$	$8.65 \pm 0.2$	$0.78 \pm 0.2$	$0.718 \pm 0.1$	$4.848 \pm 0.5$

maximum voltage, respectively. The larger value of  $V_{oc}$  shows a large difference between  $E_F$  and  $E_{redox}$ . It is evident from Table 2 that the values of  $J_{sc}$ ,  $V_{oc}$ , FF, and efficiency ( $\eta$ ) for pure  $\text{TiO}_2$  are recorded as  $6.04 \text{ mA/cm}^2$ ,  $0.76 \text{ V}$ ,  $0.571$ , and  $2.622\%$ , respectively. The inclusion of 1% Cd improved the values of  $J_{sc}$  ( $7.35 \text{ mA/cm}^2$ ),  $V_{oc}$  ( $0.762 \text{ V}$ ), FF ( $0.653$ ), and  $\eta$  ( $3.66\%$ ). The increase in the value of  $J_{sc}$  is attributed to the transfer of electrons from the HOMO of dye to the LUMO of  $\text{TiO}_2$ , which is the active contact between 1%  $\text{Cd-TiO}_2$  and dye molecules.

The heterostructure materials with  $\text{TiO}_2$  riding the cores have a higher absorption capacity due to their high porosity [36]. This is due to the improved adhesion to cores and the increased dye load capacity [37]. Porous nano-meso-microstructures with  $\text{Cd-TiO}_2@$   $\text{TiO}_2$  surface characteristics are very advantageous for maximum absorbance and scattering. For the DSSC to function, a favorable environment is provided by loosely packed grains [38]. The morphological structure's relative roughness is increased by the high porosity. Roughness in  $\text{Cd-TiO}_2@$   $\text{TiO}_2$  increases both the number of active sites from the smooth photovoltaic activity and the effective area of the film [39]. The structural arrangement's topography contributes to the photoanode semiconductor material's improved capacity for light

harvesting. Because Cd-rich sites are typically thought to be less favorable for charge production activity, this is also reflected in  $\text{Cd-TiO}_2@$   $\text{TiO}_2$ , where more  $\text{TiO}_2$  is exposed than Cd.

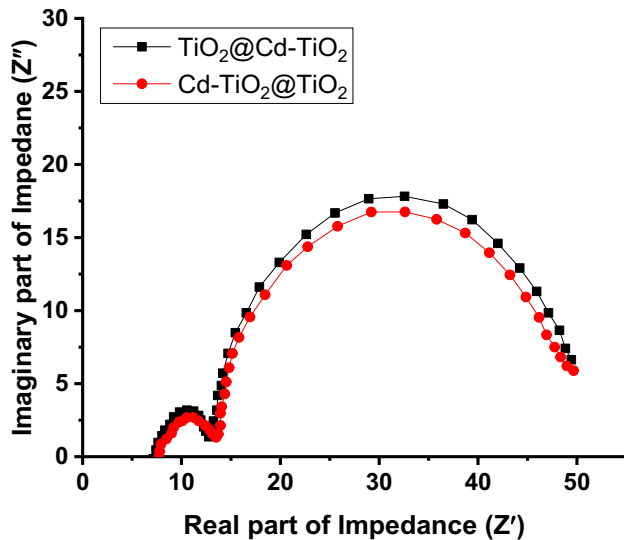
In the case of heterostructure formulism, these values are further increased and are mentioned in Table 2. The maximum value of  $\eta$  is reported for  $\text{Cd-TiO}_2@$   $\text{TiO}_2$  i.e.,  $4.848\%$ , and the corresponding values of  $J_{sc}$ ,  $V_{oc}$ , and FF are observed as  $8.65 \text{ mA/cm}^2$ ,  $0.78 \text{ V}$ , and  $0.718$  respectively. Electron trap sites produced via Cd doping prevent the recombination of electrons and holes. In  $\text{Cd-TiO}_2@$   $\text{TiO}_2$ , more trap sites are created, increasing the rate of electron injection. Heterostructure  $\text{Cd-TiO}_2@$   $\text{TiO}_2$  takes advantage of Cd as a dopant and  $\text{TiO}_2$ 's improved interaction with a sensitizer to create an environment that is favorable for rapid electron transportation. Because of the extrinsic absorption band, heterostructures are more effective at collecting light, including visible light. The photoionization of imperfections in  $\text{Cd-TiO}_2@$   $\text{TiO}_2$  results in extrinsic absorption. By creating oxygen vacancies, this photoionization increases photovoltaic activity [40]. When compared to  $\text{TiO}_2@$   $\text{Cd-TiO}_2$ ,  $\text{TiO}_2$ - $\text{Cd}@$   $\text{TiO}_2$  has better directionality and physical structure, which results in fewer grain boundary trapping sites and longer electron lifetimes, which eventually lead to higher current densities. A table of comparison of the efficiency of dye-sensitized solar cells with the published work is presented in Table 3.

### 3.8 Electrochemical impedance analysis

Electrochemical impedance spectroscopy (EIS) is a useful tool for studying the electrical properties of dye-sensitized solar cells (DSSCs) [46]. In a typical EIS experiment, a small AC voltage is applied to the cell, and the resulting current response is measured as a function of frequency.

**Table 3** Efficiency chart of dye-sensitized solar cells

Solar cell	$J_{sc}$ (mA cm <sup>-2</sup> )	$V_{oc}$ (V)	FF	Efficiency (%)	References
TiO <sub>2</sub> nanotubes array	10.3	0.84	0.54	4.7	[41]
ZnO/g-C <sub>3</sub> N <sub>4</sub> heterojunction	14.18	0.544	0.586	4.52	[42]
Sr-doped TiO <sub>2</sub> /SrTiO <sub>3</sub> heterostructures	8.42	0.80	75.5	4.70	[19]
1% Cd-TiO <sub>2</sub> /TiO <sub>2</sub>	5.55	0.73	0.609	2.47	[43]
(1% Ag + Ni <sup>2+</sup> 4 × 10 <sup>14</sup> ions/cm <sup>2</sup> )-TiO <sub>2</sub>	6.13	0.721	0.68	3.01	[44]
1%(Mn) + Ag(2 × 10 <sup>14</sup> ions-cm <sup>-2</sup> )-TiO <sub>2</sub>	5.40	0.659	0.675	2.40	[45]
Cd-TiO <sub>2</sub> @TiO <sub>2</sub>	8.65	0.78	0.718	4.848	This work

**Fig. 9** Electrochemical impedance spectroscopy of TiO<sub>2</sub>@Cd-TiO<sub>2</sub> and Cd-TiO<sub>2</sub>@TiO<sub>2</sub> photoanodes-based dye-sensitized solar cells

The EIS graph of DSSCs synthesized by coating TiO<sub>2</sub> on 1% Cd-doped TiO<sub>2</sub> (TiO<sub>2</sub>@Cd-TiO<sub>2</sub>) and 1% Cd-doped TiO<sub>2</sub> on TiO<sub>2</sub> (Cd-TiO<sub>2</sub>@TiO<sub>2</sub>) are shown in Fig. 9, indicating two semicircles in the Nyquist plot. The first semicircle is small and located near the origin, specifying the charge transfer resistance at the interface between the electrolyte and the TiO<sub>2</sub> or Cd-doped TiO<sub>2</sub> electrode [47]. This resistance is related to the recombination of electrons and holes at the interface, which can limit the overall efficiency of the solar cell [48]. The large semicircle away from the origin is associated with the impedance of the charge transfer at the counter electrode/electrolyte interface, which is typically composed of a platinum electrode and an electrolyte solution [49]. This impedance is mainly determined by the diffusion of the redox couple and the resistance of the electrolyte. Thus, the EIS results suggest that this layered structure has a significant impact on the electrical properties of the DSSCs, which can potentially lead to improved efficiency compared to the TiO<sub>2</sub>-only DSSCs.

## 4 Conclusion

Here, we have synthesized the pure and Cd-doped TiO<sub>2</sub> materials and their heterostructures as electrode materials for dye-sensitized solar cells. These materials were synthesized using the sol-gel method and are found to be pure, highly stable, and very suitable as electrode materials for solar cell applications. The formation of stable anatase phases in pristine TiO<sub>2</sub>, 1% Cd-doped TiO<sub>2</sub>, TiO<sub>2</sub>@Cd-TiO<sub>2</sub>, and Cd-TiO<sub>2</sub>@TiO<sub>2</sub> heterostructures was ascertained using the X-ray diffraction method. The incorporation of Cd insignificantly affected the lattice parameters, whereas in the case of heterostructure formulation, a prominent tunability in structural parameters was observed. Well-shaped spherical nanoparticles with an average size of 53 nm were observed in the case of pure and Cd-doped TiO<sub>2</sub>; however, in the case of heterostructures, these grains took the shape of stacked layer-like morphologies, which is favorable for the photo-absorbing functionality of these materials. These compositions respond to light very actively in the IR region and are exposed to the maximum absorbance and transmission in this region. In addition, the photovoltaic performance revealed that Cd-TiO<sub>2</sub>@TiO<sub>2</sub> heterostructures exhibited a maximum efficiency of 4.848% with a fill factor value of 0.718, which makes this composition a potential candidate as an electrode material for dye-sensitized solar cells.

**Acknowledgements** This research was supported by Princess Nourah bint Abdulrahman University Researchers Supporting Project number (PNURSP2024R327), Princess Nourah bint Abdulrahman University, Riyadh, Saudi Arabia. The authors extend their appreciation to the Deanship of Research and Graduate Studies at King Khalid University for funding this work through Large Research Project under grant number RGP2/207/45.

**Data availability** Data will be made available on request.

## Declarations

**Conflict of interest** The authors have no conflict of interest related to this publication.

## References

1. T.J. Ajayi et al., Heterodimetallic ferrocenyl dithiophosphate complexes of nickel(II), zinc(II) and cadmium(II) as sensitizers for TiO<sub>2</sub>-based dye-sensitized solar cells. *ChemistrySelect* **4**(25), 7416–7424 (2019)
2. S. Suhaimi et al., Materials for enhanced dye-sensitized solar cell performance: electrochemical application. *Int. J. Electrochem. Sci.* **10**(4), 2859–2871 (2015)
3. W.Y. Park, Y.T. Park, K.T. Lee, Systematic analysis of TiO<sub>2</sub> compact layer effect on the performance of dye-sensitized solar cells. *J. Korean Ceram. Soc.* **60**(6), 905–917 (2023)
4. S. Prasanthkumar, L. Giribabu, Recent advances in perovskite-based solar cells. *Curr. Sci.* **111**(7), 00113891 (2016)
5. W.C. Oh, Y. Areeerob, Modeling dye-sensitized solar cells with graphene based on nanocomposites in the Brillouin zone and density functional theory. *J. Korean Ceram. Soc.* **58**, 50–61 (2021)
6. S. Mahalingam, F.W. Low, A. Omar, A. Manap, N.A. Rahim, C.H. Tan et al., Zinc oxide/graphene nanocomposite as efficient photoelectrode in dye-sensitized solar cells: recent advances and future outlook. *Int. J. Energy Res.* **46**(6), 7082–7100 (2022)
7. G. Han, S. Zhang, P.P. Boix, L.H. Wong, L. Sun, S.Y. Lien, Towards high efficiency thin film solar cells. *Prog. Mater. Sci.* **87**, 246–291 (2017)
8. S.N. Karthick, K.V. Hemalatha, S.K. Balasingam, F. Manik Clinton, S. Akshaya, H.J. Kim, Dye-sensitized solar cells: history, components, configuration, and working principle, in *Interfacial engineering in functional materials for dye-sensitized solar cells*. (Wiley, Hoboken, 2019), pp.1–16
9. T. Manzoor, A.H. Pandith, Enhancing the photoresponse by CdSe-dye-TiO<sub>2</sub>-based multijunction systems for efficient dye-sensitized solar cells: a theoretical outlook. *J. Comput. Chem.* **40**(28), 2444–2452 (2019)
10. H. Chen, J.M. Cole, G.B. Stenning, A. Yanguas-Gil, J.W. Elam, L. Stan, Y. Gong, Imaging dye aggregation in MK-2, N3, N749, and SQ-2 dye... TiO<sub>2</sub> interfaces that represent dye-sensitized solar cell working electrodes. *ACS Appl. Energy Mater.* **3**(4), 3230–3241 (2020)
11. N. B. Manz, Optimizing the combination of natural pigments for co-sensitization of panchromatic TiO<sub>2</sub> dye sensitized solar cells. Doctoral dissertation, New Mexico Institute of Mining and Technology (2022)
12. S. Karthick et al., Dye-sensitized solar cells: history, components, configuration, and working principle, in *Interfacial engineering in functional materials for dye-sensitized solar cells*. (Wiley, Hoboken, 2019), pp.1–16
13. N. Ullah et al., Pyrocatechol violet sensitized cadmium and barium doped TiO<sub>2</sub>/ZnO nanostructures: As photoanode in DSSC. *Mater. Sci. Semicond. Process.* **135**, 106119 (2021)
14. M. Motlak et al., Cd-doped TiO<sub>2</sub> nanofibers as effective working electrode for the dye sensitized solar cells. *Mater. Lett.* **246**, 206–209 (2019)
15. S. Ansari et al., Effect of flower extracts on the optoelectronic properties of Cd and Sn doped TiO<sub>2</sub> nanopowder. *Sci. Adv. Mater.* **4**(7), 763–770 (2012)
16. E. Thimsen, N. Rastgar, P. Biswas, Nanostructured TiO<sub>2</sub> films with controlled morphology synthesized in a single step process: performance of dye-sensitized solar cells and photo watersplitting. *J. Phys. Chem. C* **112**(11), 4134–4140 (2008)
17. R. Mane et al., An effective use of nanocrystalline CdO thin films in dye-sensitized solar cells. *Sol. Energy* **80**(2), 185–190 (2006)
18. M.E. Yeoh, K.Y. Chan, Recent advances in photo-anode for dye-sensitized solar cells: a review. *Int. J. Energy Res.* **41**(15), 2446–2467 (2017)
19. R. Tang, L. Yin, Enhanced photovoltaic performance of dye-sensitized solar cells based on Sr-doped TiO<sub>2</sub>/SrTiO<sub>3</sub> nanorod array heterostructures. *J. Mater. Chem. A* **3**(33), 17417–17425 (2015)
20. J. Balamurugan et al., Nitrogen-doped graphene nanosheets with FeN core-shell nanoparticles as high-performance counter electrode materials for dye-sensitized solar cells. *Adv. Mater. Interfaces* **3**(1), 1500348 (2016)
21. A. Sattar, Temperature dependence of the electrical resistivity and thermoelectric power of rare earth substituted Cu–Cd ferrite. *Egypt. J. Solids* **6**(2), 113–122 (2003)
22. J. Gupta, D. Bahadur, Modulation in band gap and efficient charge separation in Cd substituted ZnO quantum dots with enhanced photocatalytic and antibacterial activity. *Mater. Res. Express* **6**(4), 045058 (2019)
23. V. Guerin et al., Electrodeposited nanoporous versus nanoparticulate ZnO films of similar roughness for dye-sensitized solar cell applications. *ACS Appl. Mater. Interfaces* **2**(12), 3677–3685 (2010)
24. A. Ahliha et al., The chemical bonds effect of anthocyanin and chlorophyll dyes on TiO<sub>2</sub> for dye-sensitized solar cell (DSSC). *J. Phys. Conf. Ser.* **909**, 012013 (2017)
25. W. Li, Influence of electronic structures of doped TiO<sub>2</sub> on their photocatalysis. *Phys. Status Solidi RRL* **9**(1), 10–27 (2015)
26. A. Kafizas et al., Where do photogenerated holes go in anatase: rutile TiO<sub>2</sub>? A transient absorption spectroscopy study of charge transfer and lifetime. *J. Phys. Chem. A* **120**(5), 715–723 (2016)
27. L. Bastonero et al., Boosted solar light absorbance in PdS2/PtS2 vertical heterostructures for ultrathin photovoltaic devices. *ACS Appl. Mater. Interfaces* **13**, 43615–43621 (2021)
28. D.H. Kim et al., Transmittance optimized nb-doped TiO<sub>2</sub>/Sn-doped In<sub>2</sub>O<sub>3</sub> multilayered photoelectrodes for dye-sensitized solar cells. *J. Solar Energy Mater. Solar Cells* **96**, 276–280 (2012)
29. L. Preethi et al., Optical transmittance and electrocatalytic efficacy of chronoamperometrically and chronopotentiometrically deposited platinum electrodes for DSSC application. *J. Nanosci. Nanotechnol.* **16**(9), 10087–10096 (2016)
30. C. Aydin, Synthesis of Pd: ZnO nanofibers and their optical characterization dependent on modified morphological properties. *J. Alloy. Compd.* **777**, 145–151 (2019)
31. C. Aydin et al., Facile synthesis, electrical and optical properties of Cu-doped GaN nanorods by sol-gel technique. *J. Sol-Gel Sci. Technol.* **78**(1), 68–75 (2016)
32. H. Aydin, Electrical and optical properties of titanium dioxide-carbon nanotube nanocomposites. *J. Nanoelectron. Optoelectron.* **9**(5), 608–613 (2014)
33. J.A. Najim, J.M. Rozaiq, Effect Cd doping on the structural and optical properties of ZnO Thin Films. *Int. Lett. Chem. Phys. Astr.* **10**, 137–150 (2013)
34. J.C. Yu et al., Effects of F-doping on the photocatalytic activity and microstructures of nanocrystalline TiO<sub>2</sub> powders. *Chem. Mater.* **14**(9), 3808–3816 (2002)
35. M. Mohammadi et al., Improved efficiency of dye-sensitized solar cells by design of a proper double layer photoanode electrodes composed of Cr-doped TiO<sub>2</sub> transparent and light scattering layers. *J. Sol-Gel Sci. Technol.* **67**(1), 77–87 (2013)
36. K. Xian et al., TiO<sub>2</sub> decorated porous carbonaceous network structures offer confinement, catalysis and thermal conductivity for effective hydrogen storage of LiBH<sub>4</sub>. *Chem. Eng. J.* **407**, 127156 (2021)
37. N. Popa, M. Visa, New hydrothermal charcoal TiO<sub>2</sub> composite for sustainable treatment of wastewater with dyes and cadmium cations load. *Mater. Chem. Phys.* **258**, 123927 (2021)
38. A. Duta, TiO<sub>2</sub> thin layers with controlled morphology for ETA (extremely thin absorber) solar cells. *Thin Solid Films* **511**, 195–198 (2006)

39. W. Pingxiao et al., Preparation and photocatalysis of TiO<sub>2</sub> nanoparticles doped with nitrogen and cadmium. *Mater. Chem. Phys.* **103**(2–3), 264–269 (2007)
40. D. Li et al., Visible-light-driven photocatalysis on fluorine-doped TiO<sub>2</sub> powders by the creation of surface oxygen vacancies. *Chem. Phys. Lett.* **401**(4–6), 579–584 (2005)
41. M. Paulose, K. Shankar, O.K. Varghese, G.K. Mor, C.A. Grimes, Application of highly-ordered TiO<sub>2</sub> nanotube-arrays in heterojunction dye-sensitized solar cells. *J. Phys. D Appl. Phys.* **39**(12), 2498 (2006)
42. D. Das, P. Nandi, ZnO/g-C<sub>3</sub>N<sub>4</sub> heterostructures: synthesis, characterization and application as photoanode in dye sensitized solar cells. *Sol. Energy Mater. Sol. Cells* **248**, 112002 (2022)
43. M.I. Khan, S. Mumtaz, G.M. Mustafa, M. Amami, U. Shahzad, E.A. Al-Abbad, Improving the current density and reducing the recombination rate of dye sensitized solar cells by modifying the band gap of titania using novel heterostructures. *Opt. Mater.* **140**, 113780 (2023)
44. M.I. Khan, N. Fatima, G.M. Mustafa, M. Sabir, S.A. Abubshait, H.A. Abubshait et al., Improved photovoltaic properties of dye sensitized solar cells by irradiations of Ni<sup>2+</sup> ions on Ag-doped TiO<sub>2</sub> photoanode. *Int. J. Energy Res.* **45**(6), 9685–9693 (2021)
45. M.I. Khan, B. Mehmood, G.M. Mustafa, K. Humaiyoun, N. Alwadai, A.H. Almuqrin et al., Effect of silver (Ag) ions irradiation on the structural, optical, and photovoltaic properties of Mn-doped TiO<sub>2</sub> thin films based dye-sensitized solar cells. *Ceram. Int.* **47**(11), 15801–15806 (2021)
46. A. Omar, M.S. Ali, N. Abd Rahim, Electron transport properties analysis of titanium dioxide dye-sensitized solar cells (TiO<sub>2</sub>-DSSCs) based natural dyes using electrochemical impedance spectroscopy concept: a review. *Sol. Energy* **207**, 1088–1121 (2020)
47. U.A. Kamarulzaman, A. Rahman, M.Y.A.A.A. Su'aitUmar, Effect of annealing treatment on multilayer TiO<sub>2</sub> films on the performance of dye-sensitized solar cells. *Optik* **218**, 164976 (2020)
48. K. Zhu, S.R. Jang, A.J. Frank, Impact of high charge-collection efficiencies and dark energy-loss processes on transport, recombination, and photovoltaic properties of dye-sensitized solar cells. *J. Phys. Chem. Lett.* **2**(9), 1070–1076 (2011)
49. W. Sun, X. Sun, T. Peng, Y. Liu, H. Zhu, S. Guo, X.Z. Zhao, A low cost mesoporous carbon/SnO<sub>2</sub>/TiO<sub>2</sub> nanocomposite counter electrode for dye-sensitized solar cells. *J. Power. Sources* **201**, 402–407 (2012)

**Publisher's Note** Springer Nature remains neutral with regard to jurisdictional claims in published maps and institutional affiliations.

Springer Nature or its licensor (e.g. a society or other partner) holds exclusive rights to this article under a publishing agreement with the author(s) or other rightsholder(s); author self-archiving of the accepted manuscript version of this article is solely governed by the terms of such publishing agreement and applicable law.